Laminar boundary layer over a flat plate at zero incidence

M. Andrejašič

University of Nova Gorica, Vipavska 11c, 5270 Ajdovščina, Slovenia

Abstract

In this paper elementary theoretical estimations of boundary-layer thickness and drag coefficient for laminar flow over a flat plate are presented. It is shown that by equating the inertial and viscous forces in the boundary layer and making some simple proportionalities, basic approximations of boundary-layer thickness and drag coefficient can be obtained. The results tell us that the boundary-layer thickness for laminar flow increases with distance from the leading edge of the flat plate and decreases with Reynolds number. The drag coefficient depends only on the Reynolds number and varies with it inversely. These estimations can quickly give us the first conclusions of dependences between the variables of interest.

Keywords: boundary-layer thickness, laminar flow, drag coefficient
PACS: 47.15.Cb

1. Introduction

The aim of this paper is theoretical derivation of elementary estimations of boundary-layer thickness and drag coefficient for laminar flow over a flat plate at zero incidence. We show that the boundary-layer thickness and drag coefficient both dependent on the same variable, Reynolds number Re [1], and both decrease with it. We also show that boundary-layer thickness increases with distance from the leading edge of the plate. Paper is round up with the comparison of derived theory and measurements [2, 3]. It shows that theory and experiments are very close at high Reynolds numbers ($Re > 10^4$).

Email address: matej.andrejasic@gmail.com (M. Andrejašič)

To describe flow of fluid with low viscosity value (high Reynolds number), in many applications the limiting solution $Re = \infty$ is a good approximation [4]. On the other hand it is useless when faced with the problem of calculating the drag of the body (D'Alembert's paradox [5]), because the no-slip condition is not satisfied, i.e. the velocities at the wall are not zero but are finite. In order to satisfy the no-slip condition, the viscosity must be taken into account. This takes care of the velocity transition from the limiting solution $Re = \infty$ close to the wall to the value of zero directly at the wall. At large Reynolds numbers, this transition takes place in a thin layer close to the wall, called the boundary layer [6]. As will be shown, the boundary layer is thinner the higher the Reynolds number, i.e. the smaller the viscosity.

The concept of boundary layer, therefore, implies that flows at high Reynolds numbers can be divided into two unequally large regions. In the major region of the flow, the viscosity can be neglected, and the flow corresponds to the inviscid limiting solution. The second region is the very thin boundary layer at the wall where viscosity must be taken into account. This division of the flow into two regions leads to considerable simplifications in the theoretical treatment of high Reynolds number flows.

Two different flow forms can occur in the boundary layer. The flow can be laminar or turbulent. We will deal only with laminar flow in this paper.

2. Estimation of the boundary-layer thickness

If a flat plate is put in a flow with zero incidence, the flow at the plate surface is slowed down because of the friction. This region of slowed down flow becomes even larger, since more and more fluid particles are caught up by the retardation. The thickness of the boundary layer $\delta(x)$ is therefore a monotonically increasing function of x. This increase of slowed down flow is schematically shown in Figure 1.

The transition from boundary-layer flow to outer flow, at least in the case of laminar flow, takes place continuously. That means that a precise boundary can not be given. It is often used in practice, that the boundary is at the point where the velocity reaches a certain percentage of the outer velocity, e.g. 99% (δ_{99}).

The boundary-layer thickness for laminar flows can be easily estimated as follows: in the boundary layer the inertial forces and the friction forces are in equilibrium. The inertial force per unit volume is equal to $\rho du/dt$, where u is the velocity component in x direction, d/dt is the substantial derivative

and ρ is the density of the flow. For steady flow this can also be written as $\rho \partial u/\partial x \cdot dx/dt = \rho u \partial u/\partial x$. For flat plate of length x, $\partial u/\partial x$ is proportional to U_∞/x, where U_∞ is the velocity of the outer undisturbed flow. Thus the inertial force is of the order of magnitude $\rho U_\infty^2/x$.

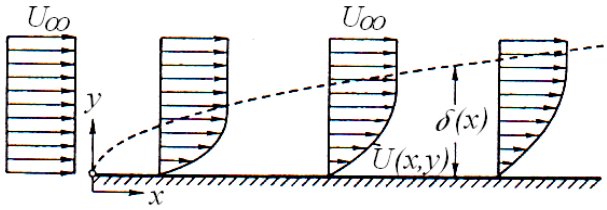

Figure 1: Boundary layer at flat plate at zero incidence is monotonically increasing with x. There is a constant velocity distribution with magnitude of U_∞ in front of the plate, but at the plate, because of the viscosity of the fluid, the flow slows down [4].

On the other hand, an expression for the friction force can easily be derived from Newton's law of friction that states that share stress is defined as $\tau = \mu du/dy$, where μ is viscosity of the fluid. We can compute the friction force as the sum of all shear forces on the volume element in the direction of the flow [4]. Friction force per unit volume is then equal to $\partial \tau/\partial y$, and for laminar flow this is equal to $\mu \partial^2 u/\partial y^2$ [4]. Velocity gradient perpendicular to the wall $\partial u/\partial y$ is of order of magnitude U_∞/δ, so that for the friction force per unit volume $\partial \tau/\partial y \sim \mu U_\infty/\delta^2$. By making the inertial and friction forces equal, we reach the relation

$$\mu \frac{U_\infty}{\delta^2} \sim \frac{\rho U_\infty^2}{x}. \tag{1}$$

The unknown equality factor remaining in this equation can be determined from the exact solution [7]. The expression for boundary-layer thickness at a plate at zero incidence is then:

$$\delta_{99} = 5\sqrt{\frac{\mu x}{U_\infty}}. \tag{2}$$

Using the expression for Reynolds number $Re = \rho U_\infty l/\mu$, the dimensionless boundary-layer thickness with respect to plate length l becomes:

$$\frac{\delta_{99}}{l} = \frac{5}{\sqrt{Re}}\sqrt{\frac{x}{l}}, \tag{3}$$

It can be seen from Equation (3) that the boundary-layer thickness decreases with increasing Reynolds number, so that in the limiting case $Re = \infty$ the boundary layer vanishes. In addition it is also seen from this equation that the boundary-layer thickness grows in proportion to $\sqrt{x}$.

3. Estimation of the friction forces

The wall shear stress defined as $\tau_w = \mu(\partial u/\partial y)_w$, where the index w denotes the value at the wall, and thus the entire friction drag of the plate can also be estimated. Using $\partial u/\partial y \sim U_\infty/\delta$ we find $\tau_w \sim \mu U_\infty/\delta$, and inserting the value of δ expressed from Equation (1),

$$\tau_w \sim \mu U_\infty \sqrt{\frac{\rho U_\infty}{\mu x}} = \sqrt{\frac{\mu \rho U_\infty^3}{x}}. \tag{4}$$

Therefore the wall shear stress is proportional to $U_\infty^{3/2}$ and also to $1/\sqrt{x}$. The wall shear stress of a flat plate is therefore not a constant, but a function which decreases monotonically with x. The shear stresses are particularly large close to the leading edge of the plate. From $\tau_w \sim \mu U_\infty/\delta$ it follows that the wall shear stress is inversely proportional to the boundary-layer thickness, i.e. the thinner the boundary layer the higher the wall shear stress. By rearranging Equation (4) using the Reynolds number definition and including the constant of proportionality determined from the exact solution [4], we get

$$\tau_w(x) = 0.664 \frac{\rho}{2} U_\infty^2 \sqrt{\frac{l}{x}} \frac{1}{\sqrt{Re}}. \tag{5}$$

If we know the relation $\tau_w(x)$, integration can be used to determine the entire friction drag. A plate wetted on one side with width b and length l has a friction drag of

$$D = b \int_0^l \tau_w(x) dx. \tag{6}$$

The drag coefficient related to the wetted surface $S = b \cdot l$ can be written as

$$c_D = \frac{D}{\frac{\rho}{2} U_\infty^2 b l} = \frac{1.328}{\sqrt{Re}} \tag{7}$$

This drag law is depicted in Figure 2. The asymptotic character of this law can be seen, and for laminar flow at Reynolds numbers $Re > 10^4$ the measurements are very close to the theory.

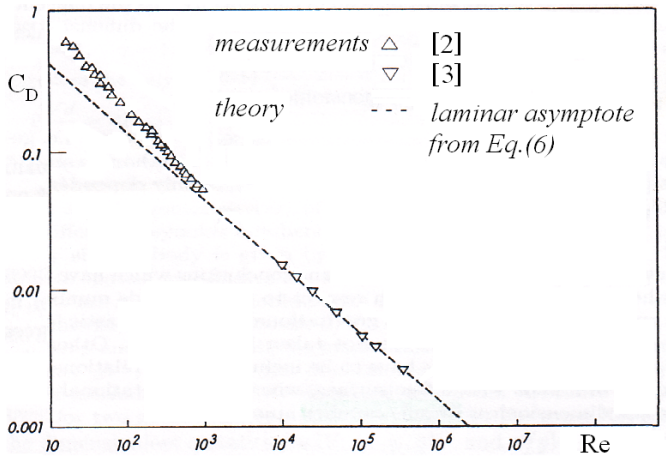

Figure 2: Dependence of drag coefficients of flat smooth plates at zero incidence on the Reynolds number. There is good agreement between presented theory and measurements for laminar flow at high Reynolds numbers [4].

4. Conclusion

In this paper it is shown, that we can easily get first estimations of boundary-layer thickness and friction forces for laminar flow at large Reynolds numbers past the flat plate with zero incidence. The boundary-layer thickness increases with distance from the leading edge of the plate and decreases with Reynolds number. The drag coefficient also decreases with Reynolds number. These results give us the first approximation that can be upgraded with improved theory [4].

References

[1] L. D. Landau in E. M. Lifshitz, *Fluid mechanics, 2nd edition: Volume 6 (Course of theoretical physics)* (Butterworth Heinemann, Oxford, 2000)

[2] Z. Janour, *Resistance of a plate in parallel flow at low Reynolds numbers* (NACA-TM-1316)

[3] K. E. Schoenherr, *Resistance of plates* (Transactions Society Naval Architects MArine Eng., Vol. 40)

[4] H. Schlichting, K. Gersten, *Boundary layer theory, 8th edition* (Springer, Germany, 2000)

[5] J. D. Anderson, Jr., *Fundamentals of aerodynamics, 4th edition* (McGraw-Hill, New York, 2007)

[6] L. Prandtl, *Uber flussigkeitsbewegungen bei sehr kleiner Reibung* (Verhandlg. III. Intern. Math. Kongr. Heidelberg, 484-491, 1904)

[7] H. Blasius, *Grenzschichten in Flussigkeiten mit kleiner Reibung* (Z. Math. Physik, Bd. 56, 1-37. Engl. translation in NACA–TM-1256, 1908)

Studies of a different flow rate usage in a concentration and separation process for determination of non-ionic surfactants

Darko Peranec*

University of Nova Gorica, Vipavska cesta 11c, 5270 Ajdovščina, Slovenia

Abstract

We tested and tried to improve the established spectrometric method for determination of non-ionic surfactants. In order to shorten and accelerate the process different flows of nitrogen gas was used to check the efficiency. We consider the use of different flow rates through the column of cation exchanger and using the diversity MESH content has been verified. Samples of waste water for the measurements have been taken in the central sewage treatment plant in Ljubljana.

Keywords: spectrophotometry; non-ionic surfactants; flow rate usage; cationic exchanger
PACS: 07.89

1. Introduction

Accounting for 40% of the total surfactants in use, non-ionic surfactants have replaced the anionic detergents and have become the largest surfactant type in use [1]. Non-ionic detergents are used as domestic and industrial cleaners. To a large extent, non-ionic detergents are biodegradable. Non-ionic surface active substance (NSAS), as all surfactants, reduce the surface tension of water and have a negative impact on the ecosystem and should be constantly monitored. The present state for determination of NSAS in environmental samples is far from perfect. From several developed and adopted spectroscopic methods for the determination of NSAS, only two were retained and are still in use. Cobalt-thiocyanate method (CTAS) [2] is still used in USA, while in Europe the modified bismuth active substances (BIAS) [3] method is in use. BIAS method is also recognized and approved as ISO 7875/2 [4]. Both methods are indirect [5]. Pollution in wastewater is typically comprised of various non-ionic and also anionic and cationic detergents which are considered interfering factor and need to be removed. Any non-ionic surfactants are subject to biodegradation and need to be preserved.

*** Corresponding author at: Univerity of Nova Gorica, Slovenia.**

Tel.: +386 53315230: fax: +386 5 3315 240.

E-mail address: dperanec@gmail.com.

The 1% formaldehyde solution in addition with cooling a sample to 4°C is proved to be suitable for 5 days storage [6]. Since there is a wide diversity of NSAS produced in large amounts in the world, there is a need for faster methods for analysis of samples.

2. Experimental setup

Regular laboratory equipment and commercially available gas-stripping apparatus was used.

A solution is prepared by dissolving 100 g NaCl and 5 g NaHCO in 2 l beaker and sufficient quantity of sample is added and diluted with distilled water to 1 l. Solution is passed into the gas stripping apparatus [Fig.1] for flushing with nitrogen gas.

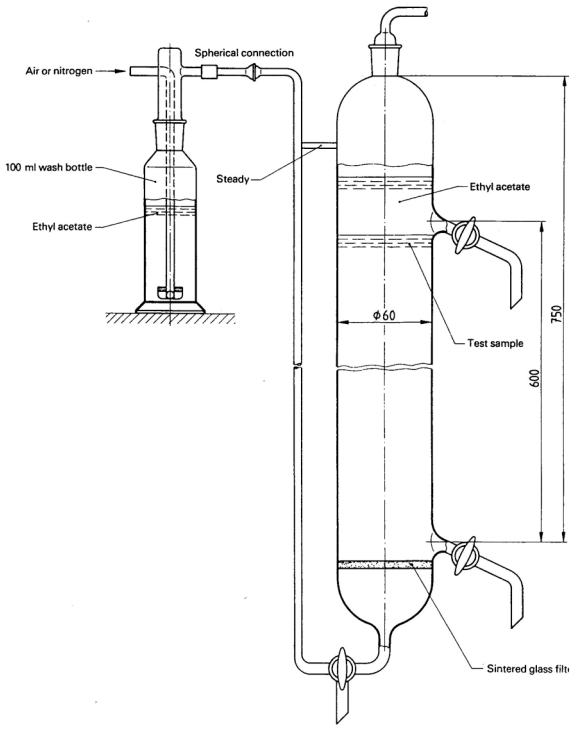

Fig. 1: Nitrogen flushing apparatus [4].
Nitrogen gas is in the first container saturated with ethyl acetate to prevent losses in the main container. With a passage of nitrogen gas through a water sample, NSAS is transferred into the added ethyl acetate. Bottom and side stopcock are made from **TFE** plug and 4- mm bore.

Nitrogen gas is passed through the sample twice for 5 minutes. Detergents are concentrated in the 100 ml of ethyl acetate. By releasing nitrogen through the sample, non-ionic and cationic surfactants if present are passed from sample to the ethyl acetate

phase. Ethyl acetate phase is collected, evaporated and replaced with 20 ml methanol. Methanol phase is passed through an ion exchange column filled with cation resin in a series of fast drops. A sample with 100 μg/L cationic surfactants Benzalkonium_chloride (BAC) in methanol was prepared for testing. Dragendorff reagent is prepared from: Solution A: 1.7 g basic bismuth nitrate and 20 g tartaric acid in 80 ml of water. Solution B: 16 g potassium iodide in 40 ml of water. Two solutions are mixed by two parts of volume of solution A with one part volume of solution B. A total of 30 ml of reagent is added to the sample and mixed for 10 minutes and left 5 minutes to activate precipitation. Solution with precipitate is filtrated through the crucible (G4) pre-washed with 2 ml glacial acetic acid. Precipitate is washed with distilled water and dissolved with 40 ml of hot (80°C) ammonium tartrate, then transferred to 100 ml calibrated flask. A total of 4 ml of EDTA was added and diluted to the mark with triple distilled water. The absorption spectra was recorded and measured on the Agilent 8453 UV-visible spectrophotometer with a 2 cm cell and 265,5 nm wavelength.

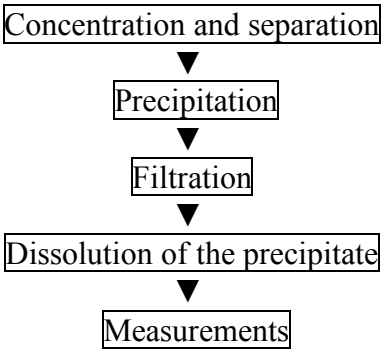

Fig. 2: Schematic representation of analysis procedure. Surfactants are collected from the water sample by sublatation with nitrogen. Only NSAS are passed through a separation column. Separated sample is then dissolved and precipitated and filtered through a crucible. Precipitate is then dissolved with ammonium tartrate and absorption spectra is measured.

3. Results and discussion

3.1. Efficiency of different flow rates of blowing nitrogen

Aim of this series of experiments was to check the losses of surfactant and ethyl acetate phase when gas stream of nitrogen was between 100-900 ml/min for 5 min passed through the apparatus. The stream of nitrogen gas must be in optimum range to ensure sufficient recovery of NSAS from sample as shown in Fig. 2. If gas flow is too intense it may lead to loss of organic phase and also a loss of NSAS.

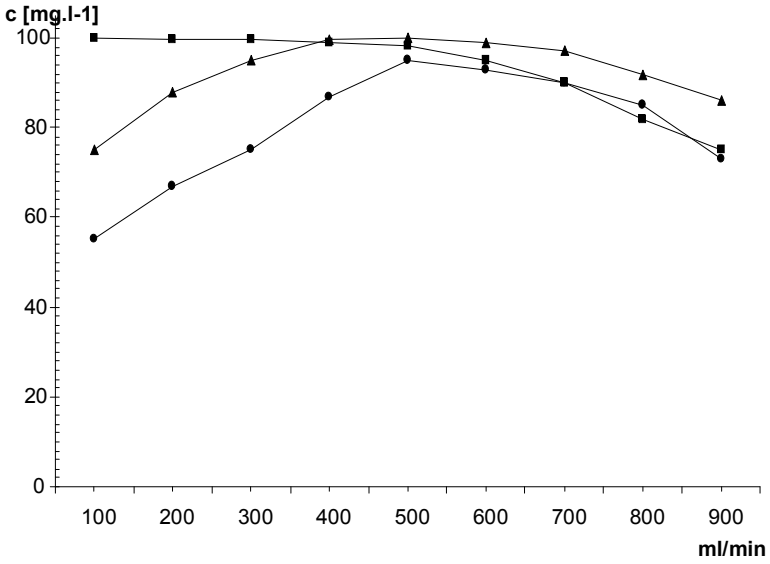

Fig.2. Effects of flow of nitrogen to the recovered amounts of Triton 100µg/l. Triton recovered from first gas-stripping (●). Total concentration recovered by second gas-stripping (▲). Residue of organic phase after gas-stripping with nitrogen (■).

Experiment results have shown that flux through a cation exchanger column should not be less than 400 and not more than 600 ml/min. For all further work, a 500 ml/min of nitrogen gas was used, as it has been demonstrated as optimum Fig.2.

3.2. Effect of ion exchange column with different fillings

To make ion exchange column as effective as possible a mixture of a different mesh of Dowex resins was prepared. A solution of three resins D25WX2, D50WX2, D100WX2 and their mixtures were tested in total of 10 grams. A sample was put through each column and effect of ion exchange resin was tested.

Table 1:
Different combinations of cation exchange resins and the resulting effects.

	D25WX2 [g]	D50WX2 [g]	D100WX2 [g]	Recovery (%)
1	10	/	/	1,5
2	/	10	/	5
3	/	/	10	15
4	5	5	/	3,5
5	/	5	5	9
6	3,3	3,3	3,3	0

Dowex ion exchange resins were mixed and tested.

Six series of experiments were performed. Columns were filled with different parts of cation exchanger. In Table 1 it is shown that number 6 is the most effective, followed by number 1. Use of only D50WX2 and D100WX2 alone was proved to be very inefficient. Mixture of three sizes cation exchanger has the longest path through a resin and was therefore most effective and used in all further work.

3.3. Measurements on efficiency of cation exchange resin was tested

Methanol phase is put through cation exchange column in a series of fast drops. Different speeds of methanol phase through a column were tested to achieve an optimum speed to eliminate any cationic surfactants residue.

Table 2:
Impact of flow on the efficiency of cationic exchange column.

Drops/ [min]	Volume [ml/min]	Cationic Surfactants [µg/l]
30	1,5	0,0
40	2	0,0
50	2,5	0,0
60	3	0,0
70	3,5	0,05
80	4	1
90	4,5	3
100	5	8
120	6	21
150	7,5	40

As shown in Table 2 flow rate through the ion exchange column affects the efficiency of cation exchange resin and shortens the process. Optimum speed through the cation exchanger is 3 ml/min or 60 Drops/min.

4. Conclusion

This paper presents a modified step in determination process for non-ionic surface active substances. The optimum stream of nitrogen gas striping the sample was proven to be 500 ml/min. If gas stream is higher, losses of Ethyl acetate phase occur as loss of NSAS.
The equal mixture of three different mesh cationic exchange resin is determined to be the most effective as shown in Table 1. Ion exchange column represent important phase in

NSAS determination although proves to be the most time consuming. Table 2 represents the optimal speed of flux through column although it is difficult to maintain a constant flow through the column. The proposed improvements represent optimal flow of nitrogen through the column and an optimal mixture of cation exchange resins for effective and fast ion exchange.

Acknowledgements

This work was supported by the International Organization for Standardization and the Committee of Scientific Research.

References

[1] [http://www.acmite.com/pdf/Sample ReadingSurfactantMarket.pdf 19.3.2007]

[2] Standard methods for the examination of water & wastewater 5540 B surfactant separation by sublation, *American Public Health Association*; 20th edition pp 5-56-5-67.

[3] R. Wickbold, Tenside Deterg., 9 (1972) 173.

[4] Water quality - Determination of surfactants – Part 2: Determination of non-ionic surfactants using Dragendorff reagent *SIST-ISO 7875/2*-1984 (E).

[5] Bogdan Wyrwas, Andrzej Szymanski, Zemon Lukaszewski, *Analytica Chimica Acta*, 278 (1993) 197-203.

[6] Andrzej Szymanski, Zbigniew Swit, Zemon Lukaszewski, *Alytica Chimica Acta*, (1995) 31-36.

Ab-initio simulation on the effect of external electric field on the band structure of NaCl crystal

C. S. Praveen*, M. Valant

University of Nova Gorica, Vipavska 11c, 5270, Ajdovščina, Slovenia

Abstract

The effect of external electric field on the band structure of NaCl crystal is simulated using a finite field perturbation scheme. The directional breakdown of the NaCl crystal is verified and the more favourable crystallographic directions are reported. The static and high frequency dielectric constants and the refractive index are simulated within a highly accurate Coupled Perturbed Kohn Sham (CPKS) theory.

PACS: 71.15Ap; 71.15Mb

Keywords: Ab- initio simulations, NaCl, Finite Field Method, CRYSTAL09, CPKS

1. INTRODUCTION

First principle study on the response properties of materials to external perturbations like electric field and magnetic field are computationally very demanding. The response of materials to external electric fields determines their dielectric properties and the derivative of the total energy with respect to the macroscopic electric field implies the nonlinear susceptibilities. In the field of electro optical applications and of laser technology, the external electric field dependence on the band structure of many ionic crystals is of considerable interest. Particularly the laser induced breakdown phenomena in wide band gap insulators are widely studied for their use in UV transmitting windows. As a typical example of a wide band gap ionic insulator, alkali halides have a pronounced participation in the field of electro optics. The directional breakdown of alkali halides in the presence of an external high electric field applied along a particular direction is widely studied both experimentally and theoretically [1, 2]. By performing first principle calculations, we aimed at getting into field dependence of the electronic band structure, the variation in optical band gaps and the directional dependence on the breakdown field in the NaCl crystal by applying electric field along three different crystallographic axes. A systematic experimental investigation on the reduction in band gap value with respect to the field applied along different direction of the crystallographic axes is quite challenging as the crystals with proper cleavage in different directions are quite hard to obtain. Because of the non periodicity of the macroscopic electric potential, the periodicity of the crystal breaks and we cannot apply the Bloch theorem for solving the equations in the self consistent field (SCF) [3, 4] procedure. This brings some limitations to study the effects computationally. The application of a sawtooth potential in conjunction with a supercell approach proposed by Kunc and Resta [3], allows maintaining

* Corresponding author.
E-mail address : mnr.praveen@ung.si

the periodicity of the crystal along the applied field. The finite field "sawtooth" scheme implemented in the CRYSTAL [4, 5] computational code has been used for the present study.

2. COMPUTATIONAL DETAILS

First principle calculations on the effect of external perturbations on the band structure of NaCl crystal is studied using the finite field sawtooth perturbation scheme implemented in the CRYSTAL code. In CRYSTAL the wave function of the solid is described in terms of crystalline orbitals; these are obtained as the Linear Combination of the Atomic Orbitals (LCAO) or localized functions associated with the atomic positions. The great advantage of this code is its ability to describe the ground state electronic structure of materials within both Hatree Fock and Kohn Sham Hamiltonians [6, 7] or various hybrid approximations.

In order to preserve the high computational accuracy, high values have been used for the cut off parameters controlling the direct space summation for the Coulomb and exchange series (7, 7, 7, 7, 14) and are explained in detail elsewhere [5,8]. The reciprocal space integration is carried out by sampling the first Brillouine zone at a regular set of points defined by the Pack-Monhrost shrinking factor [9], IS, 8 (75 sampling points). All electron basis set, taken from the CRYSTAL[†] website, are used for describing both the anion and cation. The most diffused exponents are re-optimized with respect to the Becke, three-parameter, Lee-Yang-Parr (B3LYP) [10] hybrid functional. The lattice parameters are taken from the literature [11] and are re-optimized to minimize the total energy with respect to the B3LYP functional. In order to tune the band gap of the NaCl crystal, close to the experimental value the default value of the Fock exchange (20%) in the B3LYP functional is modified to 40%. Convergence is reached while performing the SCF iteration by increasing the percentage of Fock mixing parameter. The calculation of static and optical dielectric properties was performed with a relatively accurate analytical coupled method [12]. This coupled finite filed method using the Kohn sham Hamiltonian takes the local field effects. The integrals are controlled by the tolerance factors [5, 8] of 8, 8, 8, 8 and 16. The irreducible part of the first Brillouine zone is sampled by the shrinking factor IS, 12 (108 sampling points). The threshold in the energy difference is controlled by a tolerance factor of 10 [5].

3. RESULTS AND DISCUSSION

The electronic band structure of the NaCl crystal is evaluated within an SCF procedure using the density functional theory and is reported in Figure 1. The optical direct band gap of the crystal is calculated as 8.63 eV and is in good agreement with the experimental value 8.79 eV [14]. The independent components of the static and high frequency dielectric tensor elements, polarizability, refractive index and the first order electric susceptibility are calculated using a Coupled Perturbed Kohn Sham (CPKS) scheme implemented in the latest version of CRYSTAL. All these values are reported in Table1 along with the experimental values.

[†] http://www.crystal.unito.it/Basis_Sets/Ptable.html

Lattice parameter A^0	ε_∞	ε	α Bohr^3	χ	n
5.63[a] (experimental)	2.2398 (2.25)[b]	5.3562 (5.62)[b]	29.7023	1.2398	1.4967 (1.50)[b]
5.731 (our results)	2.1909	6.0091	30.0958	1.1909	1.4802

[a] from Reference 12, [b] from Reference 13

Table 1: The static and high frequency dielectric constants (ε and ε_∞), polarizability (α), refractive index (n), and first order hyper polarizability with respect to both experimental and optimized lattice parameters. The values in the brackets show the experimental results.

In order to study the effect of electric field on the band structure of bulk NaCl crystal, electric field is applied along the three different directions of the crystal, namely <001>, <011> and <111> respectively. In each case a super cell of size four times bigger than the conventional one along the applied field direction is created. The field value is increased from 0.000 a.u[‡] to 0.050 a.u in steps of 0.0025 a.u and both the direct, E_g and indirect, E_g (indir) band gaps are evaluated for each value.

In each of the cases it is evident that all the bands are modified, both the valence band and the conduction band are shifted towards each other, and hence the band gap is decreased. For instance, the variation in the band structure for a field value of 0.0200 a.u is reported along with the zero field band structure in Figure 1. In order to study the direction dependence of the breakdown field, band gap is plotted against the applied field for the three crystallographic directions simultaneously in Figure 2. In the case of field along the <111> direction the reduction in the gap value is much faster and the material undergoes for a dielectric breakdown with a field value 0.0275 a.u. In the case of <011> direction the reduction is much slow and the material can with stand for much higher field and it undergoes breakdown over 0.05 a.u. If we look at the case of field along the 001 direction the effect is much surprising as the material changes to an indirect band gap material just over a field value of 0.01 au and remains well separated from the direct band gap values until it goes break down just over 0.04 a.u. The difference in the direct and indirect band gap values is very small, and is linearly increasing. In the case of NaCl, the <111> direction is more favourable as the crystal offers a less resistance in this path.

[‡] Conversion factor : 1 a.u = 1.71527 E+07 ESU.CM(-2) = 5.72152 E+01 C.M(-2) = 5.14226 E+11 V.M(-1)

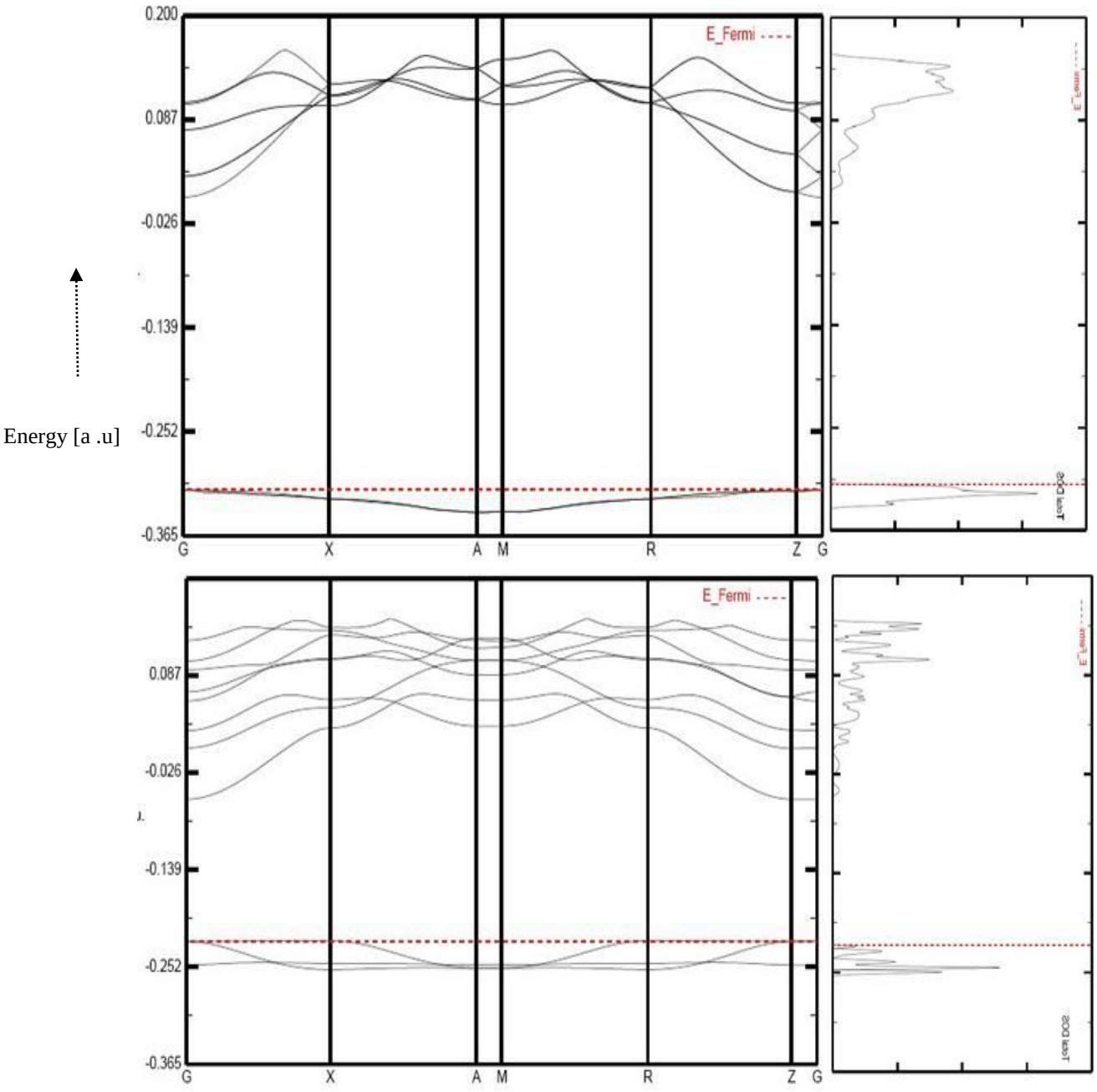

Figure 1: Band dispersion and density of states of NaCl crystal with respect to the external field along <001> direction. Top figure: Zero field; Bottom figure: 0.020 a.u field.

The directional dependence of the breakdown field for the alkali halides has already been reported and we were able to reproduce it by considering the fact that there is a small splitting in the direct and indirect band gap value as shown in Figure 2. This implies that beyond a particular field value, the breakdown path deviates from the applied field direction.

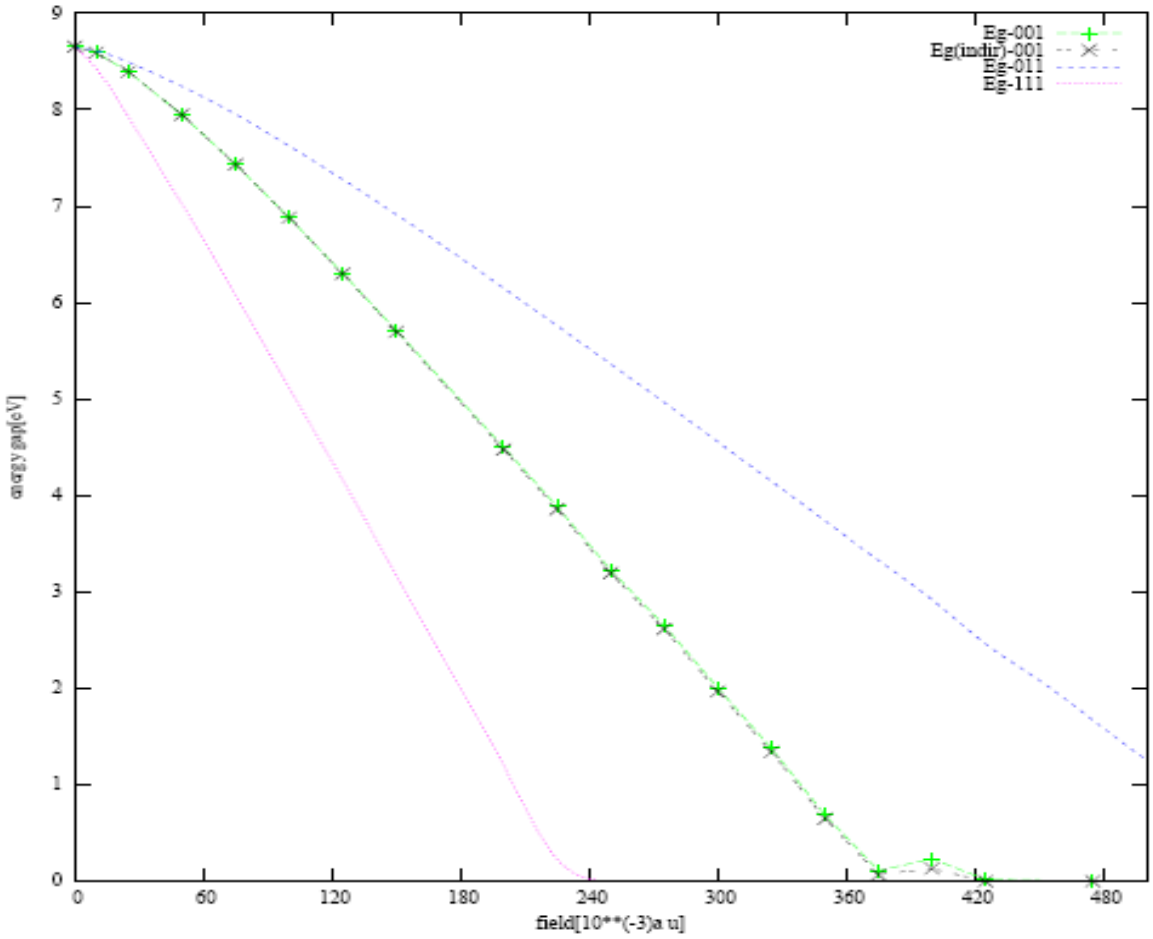

Figure 2: Variation of band gap with respect to the external field along three different crystallographic directions. E_g is the direct band gap value and E_g (indir) is the indirect band gap value.

The charge density difference with field (0.020 a.u) and without field is plotted for the <001> directions and is given in Figure 3.

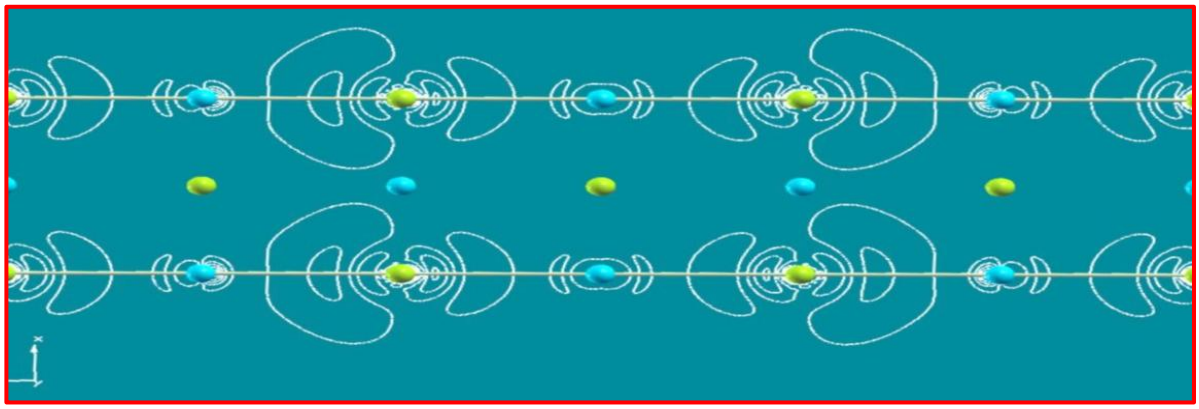

Figure 3: The charge density difference map (zero field and 0.020 a.u filed along the <001> direction) in the XZ plane.

The atoms are well polarised in the direction of the applied field and is evident that the anions (green balls) are more polarisable.

4. CONCLUSIONS

We performed a first principle DFT based simulation on the basis of finite field perturbation scheme and reported that the application of the electric field will reduce the band gap of NaCl crystal and the crystal will undergo towards a dielectric breakdown for a comparatively large field. The breakdown in alkali halides are completely directional dependent and the breakdown path has low resistance along the <111> direction. The application of electric field beyond 0.0125 a.u along the <001> direction of NaCl crystal brings it into an indirect band gap insulator. The static dielectric and optical properties are evaluated using an analytical and highly accurate Coupled Perturbed Kohn Sham scheme.

5. ACKNOWLEDGEMENTS

The work was supported by the "Young Researcher" grant of the Slovenian Research Agency. The numerical calculations were carried out by the Grid facilities, provided by Jožef Stefan Institute, Ljubljana, Slovenia.

6. REFERENCES

[1] Kaspari, M. E., *Phy. Rev*., 1955, 98, 1679.

[2] Herbert, B. C., *Phy. Rev*., 1947, 76, 1394; Kulikov, V. D., *Tech. Phys*., 2009, 54, 56.

[3] Kunc, K.; Resta, R., *Phys. Rev. Lett*., 1983, 51, 686.

[4] Darrigan, C.; Rerat, M.; Mallia, G.; Dovesi, R., *J. Comp. Chem*., 2003, 24, 1305.

[5] Dovesi, R.; Saunders, V. R.; Roetti, C.; Orlando, R.; Zicovich-Wilson, C. M.; Pascale, F.; Doll, K.; Harrison, N. M.; Civalleri, B.; Bush, I. J.; D'Arco, P.; Llunell, M., *Crystal06 user's manual*., 2006, Universita` di Torino, Torino.

[6] Hohenberg, P.; Kohn, W., *Phy. Rev*. B., 1964, 136, B864; Kohn, W.; Sham, L. J., *Phy. Rev*., 1965, 140, A1133.

[7] Ehenreich, H.; Cohen, M. H., *Phy. Rev*., 1959, 95, 786.

[8] Pisani. C.; Dovesi. R.; Roetty. C., *Lecture notes in chemistry.,* 1988, Springer-Verlag, Heidelberg.

[9] Monkhorst, H. J.; Pack, J. D., *Phy. Rev*. B., 1976, 13, 5188.

[10] Becke, A. D., *J. Chem. Phys*., 1993, 98: 5648, Lee C.; Yang W.; Parr, R. G., *Phys. Rev. B.*, 1988, 37, 785.

[11] Ferrero, M.; Rérat, M.; Orlando, R.; Dovesi, R., *J. Comp. Chem.*, 2008, 29, 1450.

[12] Bragg, W.H.; Bragg, W. L., *Phys Rev*., 1925, 25, 618.

[13] Dekker, A. J., *Solid state physics*., 2003, Prentice Hall, Englewood Cliffs, NJ.

[14] Roessler, D. M.; Walker, W. C., *Phys. Rev*., 1968, 166, 599.

First results and operations of FERMI@Elettra photo-injector

S. Spampinati.

Sincrotrone Trieste, Trieste, Italy and University of Nova Gorica, Nova Gorica

ABSTRACT

FERMI@ELETTRA is a fourth generation light source under construction and commissioning at Sinctrotrone Trieste Synchrotron light laboratory (1). It is based on a free electron laser (FEL) driven by a linear electron accelerator. This paper reports on the first commissioning stage of FERMI accelerator, on the results of the driven laser system, on the measured quantum efficiency (QE) of the photo-cathode and on the results of the photo-injector. Results of new electron beam pulse shaping experiments, showing the evolution in the gun of several electron beams distributions, are presented. We demonstrated that it is possible to shape the electron beam as required by FERMI. We have developed a simple and inexpensive cathode cleaning technique, which is easier and safer to perform comparing to ion sputtering and laser cleaning. This technique involves cleaning the cathode with ozone and it has proven to be very effective in restoring the cathode's QE.

Keywords: Photo-injector, Cathode cleaning, Longitudinal electron beam profile

PACS:29.27.Bd, 41.60.Cr,

1.INTRODUCTION

A lot of experiments in every branch of natural sciences have been realized in the last 20 years exploiting the X rays produced in the synchrotrons (2). The next evolution of X ray source will be represented by VUV (vacuum ultra-violet) and X-ray FEL (3). LCLS (linear coherent light source) (4), the first X-ray FEL in the world, is now in user operations. Others similar facilities are under realization. FERMI@ELETTRA is one of them. FERMI will use high energy electrons produced by a linear accelerator (5). The electrons are produced by the impact of a UV laser on a copper cathode placed in a first RF cavity in which the electrons are accelerated at an energy of approximately 5 MeV. Then the beam goes in two booster cavities in which it reaches an energy of 100 MeV. This first stage of the accelerator is called photo-injector. Then the beam is matched transversally in a transfer line before it enters in the first section of the linac (5). High charge for bunch, low emittance and the possibility to shape the electron beam are the key peculiarity of photo-cathode gun with respect to other electrons beam sources. The charge extracted is related to the quantum efficiency (QE) (6) of the cathode material. QE is the ratio between the charge extracted from the cathode and the laser pulse energy. The laser action reduces the quantum efficiency of the material mainly through

carbon contamination and it is important to develop methods to clean cathode. The techniques used usually are laser cleaning or ion sputtering (7). Cathode replacement is the alternative to cathode cleaning**.** During the commissioning of FERMI we have used, for the first time, an ozone bath and this appear to be a useful and simple technique. The emittance measures the beam volume in the transverse phase space. Electrons emitted from the cathode are non-relativistic. They repel each other transversally through Coulomb forces while space charge forces are meanly longitudinal for relativistic electron. A fast acceleration in the gun cavity is then important to obtain low emittance. The cathode is placed in two-cell RF cavity resonant to 2856 GHz in the TM010 π mode. The 2 μs pulse which feeds the cavity has peak power of 10 MW. The peak accelerating gradient in the gun is 100MV/m. The beam energy at the exit of the gun is approximately of 5 MeV. This energy is gained in less than 30 cm. The gun cavity is surrounded by a solenoid that compensates Coulomb repulsion in non relativistic regime. Then the beam enters in the two following booster sections placed at a distance from the gun imposed by emittance compensation scheme (8). The electron beam pulse shaping is obtained by laser pulse shaping. The Gaussian and flat top are the profile used in other free electron laser projects (9,10) while FERMI will use a ramped shape profile (11). We have tested longitudinal pulse shaping and we report it in this paper.

2. PHOTO-CATHODE LASER

Ti:sa laser is used to produce a UV laser pulse long 10 ps via harmonic triplication in a non harmonic crystal (12). The energy available in the UV is 500 pJ. The laser system is described in (13). The laser pulse is split into two beams before to go to the cathode. A pulse containing the 99% of the energy of the original one goes to the cathode while the rest of the beam is directed to a diagnostic screen monitored by a CCD. In this way it is possible to control the transverse profile homogeneity, the spot dimension and the pointing stability. The laser longitudinal profile is reconstructed by cross correlation (14). Several longitudinal laser profiles have been used during this first commissioning shape. Fig. 1 reproduces a ramped profile very close to the nominal one. The laser pulse energy available is of 500 μJ. From the control room it is possible to check the pulse energy and it is possible to reduce it with a rotating wave plate.

#simone.spampinati@elettra.trieste.it

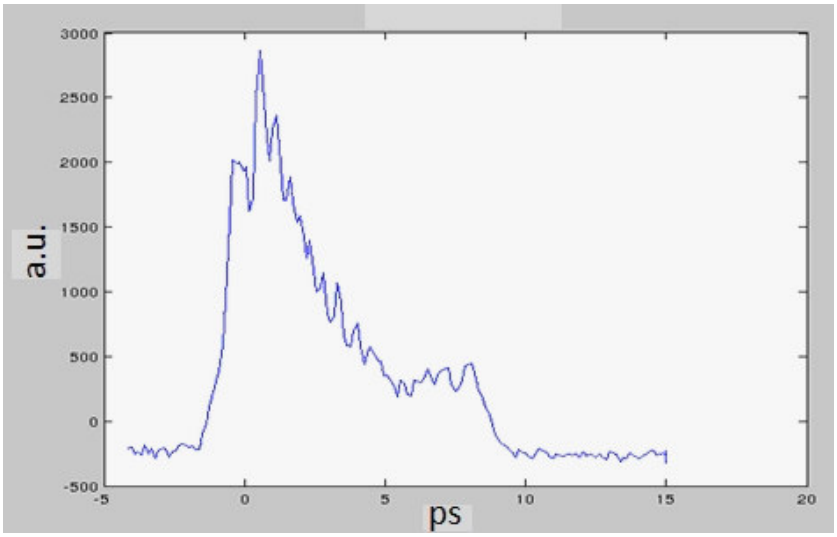

Fig. 1; Photo cathode UV laser longitudinal profile measured with cross correlation: laser intensity in arbitrary unit versus the time (beam duration) in ps.

3. GUN RESULTS

The charge extracted from the cathode, for a certain value of laser energy and quantum efficiency, depends even from the phase of the electric field seen by the electrons when the laser hit the cathode. The electrons are accelerated by the electric field for a right value of the phase and are extracted. Otherwise they are decelerated and are then not extracted. Fig. 2 reproduces a phase scan performed after 1 month of operation. The laser energy used is of 314 μJ.

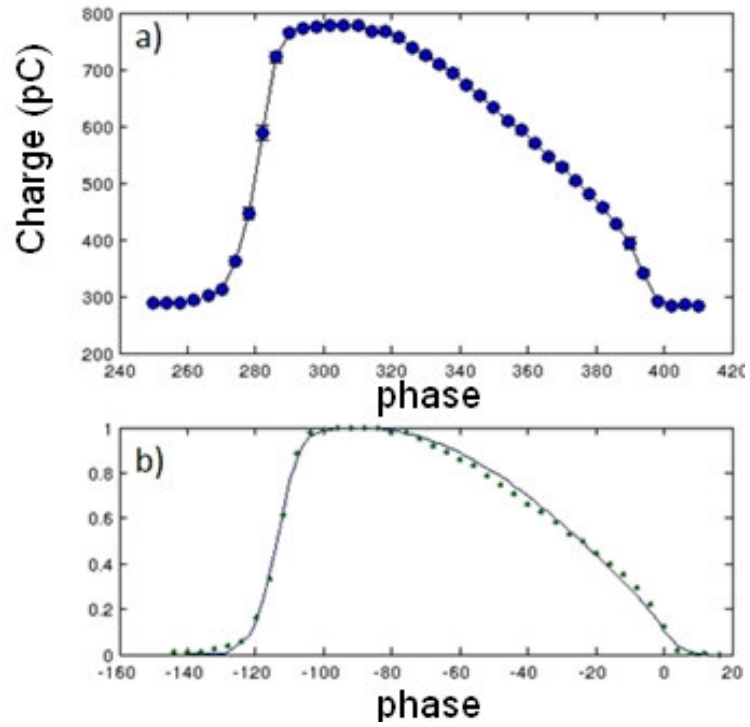

Fig. 2; Charge extracted from the cathode at laser energy of 314 micro J versus relative rf phase. The Fig. 2b reproduces the experimental curve compared with simulations (solid line). In this second picture both experimental and theoretical points are normalized to the maximum extracted charge.

It is clear from simulations that the maximum acceleration is at the point located at -35 degree from the phase from which the zero extraction region starts (-35 in the Fig 2 b). The Fig. 2 corresponds to a quantum efficiency of $1.6 \cdot 10^{-6}$ C/J at the maximum extraction phase. The electron beam energy at the maximum acceleration point has beam measured with the spectrometer placed just after the gun. The measured energy is 5.1 MeV. The beam emittance has been measured after the gun (just before the injector) with the slits method (15). The slits measurements reveal a 15% asymmetry of the emittance in the two planes.

4. CHATODE RESULTS AND CLEANING

Copper quantum efficiency reported in literature is in the range $10^{-5} - 10^{4}$ C/J hence the laser system was designed to deliver 500 μJ to produce 1nC electron bunch. During the first month of operation a fast quantum efficiency degradation has been observed as shown in Fig. 2. It is suspected that the laser pulse breaks chemical bonds in organic species contained in the high vacuum atmosphere surrounding the cathode (10^{-9} atm). Then the free carbon contaminates the cathode reducing the quantum efficiency. Carbon contamination has been detected in UV and X-ray optics in synchrotrons beam line. Synchrotron line scientists use an ozone bath to clean their optics from carbon. We have tried to do the same with the cathode. We have filled the gun with oxygen and illuminated it with a UV lamp. The UV breaks the bonds in oxygen molecules producing ozone and free oxygen. The ozone produced in this way reacts with carbon and removes it from the cathode. Phase scan before and after the cleaning are shown in Fig. 3.

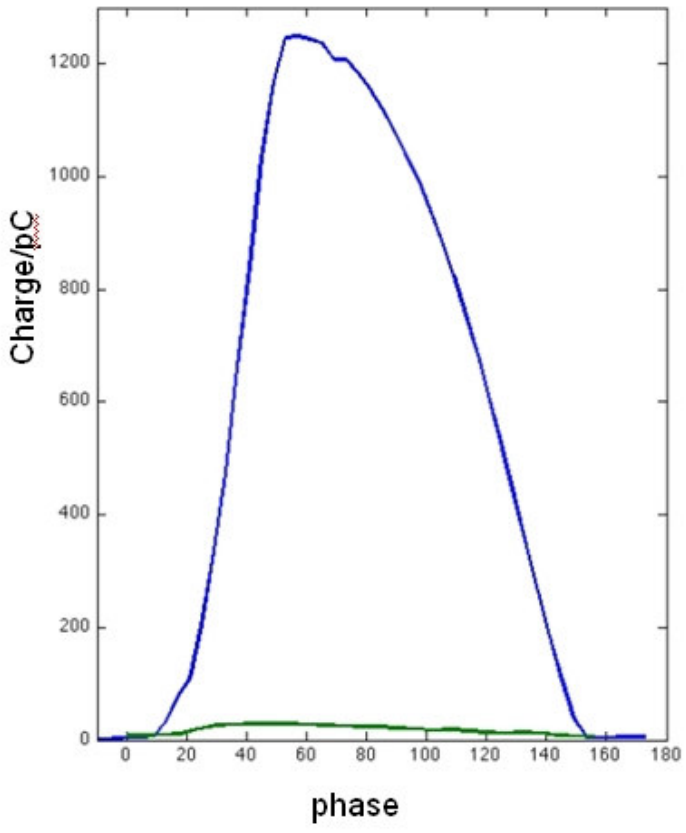

Fig. 3; phase scan before (green curve) and after cathode cleaning (blue curve).

The quantum efficiency, after the cleaning, is $8 \cdot 10^{-5}$ C/J at the maximum extraction phase and $4 \cdot 10^{-5}$ C/J at the maximum energy phase. The fig 4 shows the extracted current versus the laser energy at the operational phase before (blue curve) and after (green curve) cathode cleaning. In principle the ozone can oxidizes the gun cavity producing a bad behavior with the RF electric field. We have not seen an increase in the number of discharge after the cleaning.

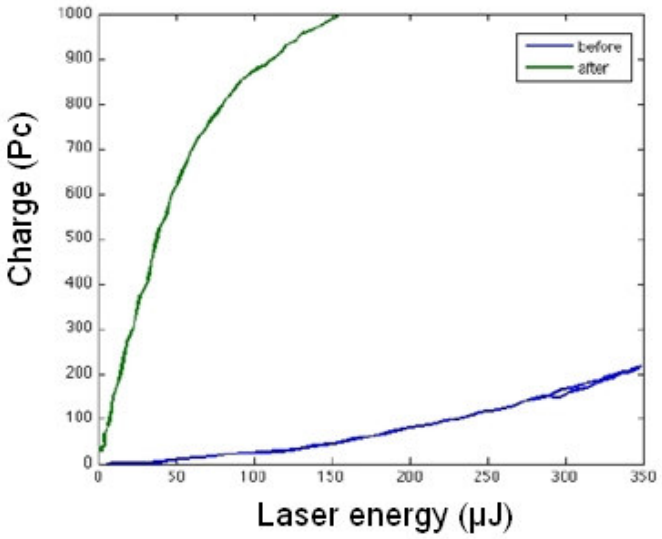

Fig (4); charge extracted versus laser pulse energy, before (blue curve) and after (green curve) cathode cleaning.

5. INJECTOR RESULTS.

The quality of the beam produced by the photo injector is measured in the transfer line. The emittance is measured with the quadrupole scan technique (16). After the injector the x emittance is 1.36 µm while the y emittance is 1 µm, so there is a 36 % asymmetry. Analysis of the growth of the asymmetries are ongoing. The maximum energy measured with a spectrometer is 102 MeV. The rms energy spread is below the 125 KeV. These values are in the designed range. The transverse jitter is below the 10 µm while the time arrival jitter is below the 1 ps. Al this results are referred to a charge of 330 pC and meets the requirements of FERMI free electron laser commissioning first stage as shown in the tab 1.

Tab1; Beam requirements and obtained parameters values.

Beam parameter	Injector results	Fel requirement
Energy	102 MeV	95-105 MeV
Energy Spread	<100 KeV	<100 KeV
Charge	330 pC	330 pC
Bunch length	5 pC	5-8 pC
Emittance	<1.36 µm	<1.5 µm
Time jitter	<1ps	200 fs
Transverse jitter	<10µm	<15 µm
Charge jitter	<1%	<3%

6. LONGITUDINAL BEAM PROFILE EXPERIMENTS.

The longitudinal profile of the electron beam at the cathode is determined by the longitudinal shape of the laser pulse longitudinal shape. The profile evolves in the gun and in the injector under the action of space charge. The simulation of the nominal ramped profile at the cathode and at 100 MeV are shown in the Fig. 5.

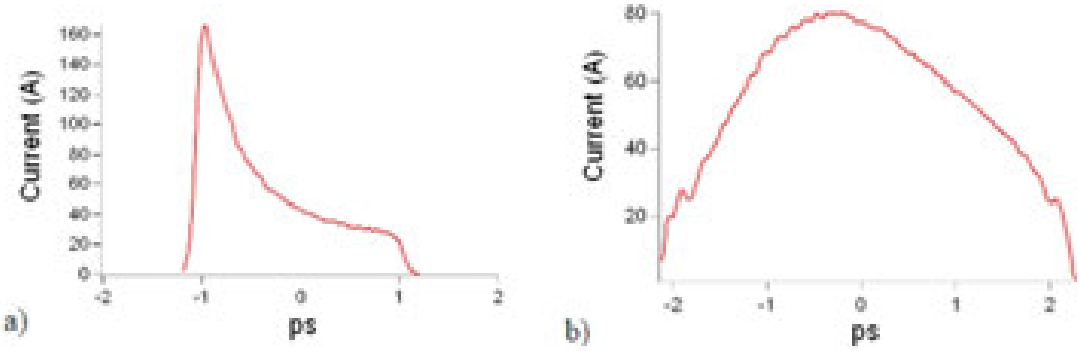

Fig. 5; Simulation of the nominal ramped profile of the electron beam current versus time (beam duration) at the cathode (a) and at the gun exit (b).

We have performed experiments to see how several initial charge distributions evolve in the gun. The longitudinal profile of the laser is measured with cross correlation method and the longitudinal profile of the electron beam after the gun has been analyzed measuring, with a streak camera, the longitudinal profile of the radiation emitted by the beam while passing a soft matter medium (Cherenkov radiator). The Fig. 6 shows the profiles of the electron beam obtained at the gun exit for different laser profiles. The nominal laser profile at the cathode and at the end of the gun are drawn in magenta, Fig. 6 c. From comparison between the nominal profile in Fig. 5 and 6 we can see that pulse shaping is going in the expected way.

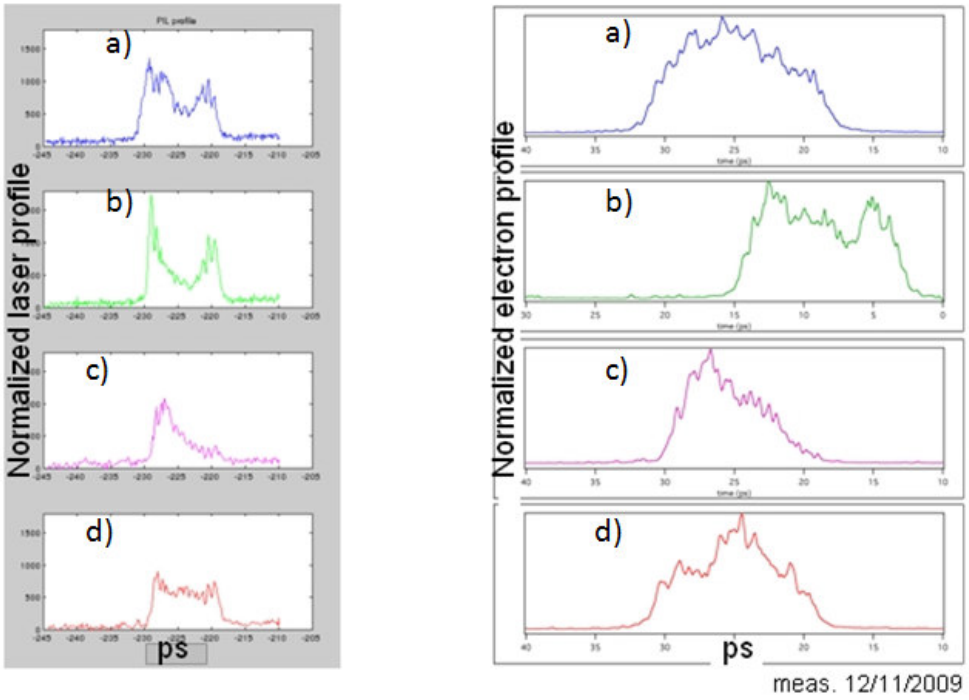

Fig. 6; Laser (left) and electrons (right) measured profiles. The Laser profile is reconstructed by cross correlation and the Electrons Profile has been reconstructed been analyzed measuring, with a streak camera, the longitudinal profile of the radiation emitted by the beam while passing a soft matter medium (Cherenkov radiator). The nominal laser profile at the cathode and at the end of the gun are drawn in magenta, Fig. 6 c.

7. CONCLUSIONS

We have reported the results of the first stage of the commissioning of FERMI@ELETTRA. The photo-injector has reached the requirements of the first stage of FERMI free electron laser commissioning. We have shown that it is possible to restore cathode QE with an ozone bath without damaging the gun. We have performed electron beam pulse shaping experiments in which we have studied the relation between laser and electron beam longitudinal profile and demonstrated that it is possible to shape the electron beam as required by FERMI@Elettra.

REFERENCES

[1] W.Barletta et al. Rivista del Nuovo Cimento della Societa Italiana di Fisica 29, 1-104 (2006).
[2] http://www.lightsources.org (18/03/02).
[3] J. Madey, United States Patent 3822410, 1974.
[4] P. Emma, Proceedings of the 2009 International FEL Conference.
[5] FERMI@ELETTRA, Conceptual Design Report. Edited by C.J.Bocchetta (2007).
[6] http://www.rp-photonics.com/quantum_efficiency.html (18/03/2010).
[7] R.Akre et al. Physical review special topic 11, 030703 (2008).
[8] M. Ferrario, J. E. Clendenin, D. T. Palmer, J.B. Rosenzweig, and L. Serafini, Report No SLAC-PUB 8400, 2000.
[9] LCLS, Conceptual Design Report SLAC-R-593 UC-414, 2002.
[10] H. Weise. Proceedings of the 2004 EPAC Conference.
[11] S.Lidia,G.Penco, M.Trovo, Report No. ST/F-TN-06/11, 2006.
[12] Robert W. Boyd, Nonlinear optics, Second edition, Academic press, 2003.
[13] M.Danailov et al. Proceedings of the 2007 International FEL Conference.
[14] R.A. Avakyan et al. Quantum Electronics 24,71 (1994).
[15] M. Zhang, Report No. Fermilab-TM-1998, 1996.
[16]H. Wiedeman, Particle Accelerator Physics, Third edition, Springer-Verlag, 2007.

Measurement of the main rheology parameters using only the flow test

J. Virc[a,*], G. Kepec[b], B. Znoj[b]
[a]University of Nova Gorica, Vipavska 11c, 5270 Ajdovščina, Slovenia
[b]Helios TBLUS d.o.o., Količevo 1, Domžale, Slovenia

Abstract
In this article the rheology parameters of paint are introduced and compared to paint application properties. Rheology parameters can be determined from the rheology flow graph and its understanding is of great importance for better prediction of paint application conditions. These conditions are important for painters and are usually closely linked to paint equipment, temperature, humidity and substrate properties. We show that the rheology properties can be predict by using only the rheology flow test without the additional two test usually used, namely the temperature test and the frequency sweep test.

Keywords: rheometer, rheology flow graph, viscosity, paint, conditions

1. Introduction

When new paint is made it is important to use all tests which can help us to finish our work in expected way. Rheology describes the deformation of a subject (in our case liquid) under the influence of shear forces [1]. Rheometry is the measuring technology which is used to determinate rheological data η - viscosity, G´- storage modulus, G˝- loss modulus. The measurement of the viscosity of liquids first requires the definition of the parameters which are involved in the flow [2]. For laminar, ideal viscous flow the difference in velocity between neighboring layers is the same (dv = const) since the velocity v (h - thickness) decreases linearly in the gap between the plates in rheometer (Figure 1). All layers are assumed to have the same thickness (dh = const) (Figure 1). Therefore, it follows that the shear rate $\dot{\gamma}$ is constant for every point between the plates because: $\dot{\gamma}$ = dv/dh = const (Figure 1).

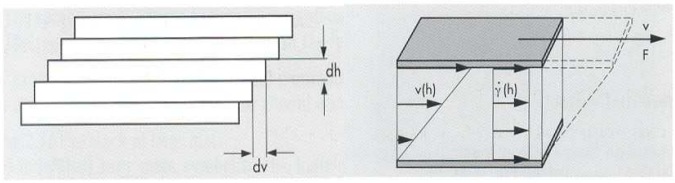

Figure 1: On the left are seen flowing layers, which in laminar flow has the same h-thickness. On the right is shown connection between velocity and shear rate (also in the shear gap of rheometer Figure 2). Laminar flow is used in our three tests. *Figure taken from reference 1.*

Both $\dot{\gamma}$ and v provide information about the velocity of the flowing fluid and the advancing of flowing fluid. The advantage of the shear rate is that it shows a constant value throughout the shear gap, which is therefore independent of the position of the flowing layer (Figure 1).

* Corresponding author.
Email address: janez.virc@gmail.com (J. Virc)

In all fluids, there are frictional forces between the molecules and, therefore, they display a certain flow resistance which can be measured as viscosity. We would like to explain the rheology parameters of the paint that can be determined by rheology flow graph and appearance to the application characteristics of the paint. We saw that measuring rheology flow test is the only test need to do for solvent decorative paint. The main rheology tests are temperature test, frequency sweep test and flow test.
In this article explanation is made on two samples. It is explained what rheology flow test shows and how is that seen on temperature and frequency sweep test.

2. Experimental setup

Measured sample was a decorative paint with a content of VOC – volatile organic compound less than 400 g/l [3, 4]. The characteristics were determined by the brush application. All measurements were done with rheometer (producer Anton Paar) by cone-and-plate measuring system (Figure 2). Several measuring systems are available for determining paint properties: Coaxial cylinder, Double-gap, Parallel-palate, Mooney/Ewart measuring systems. For our samples it was enough to use a cone and plate system which was standardized in 1976 as DIN 53018 and adopted more or less completely in 1993 as ISO 3219 [1].

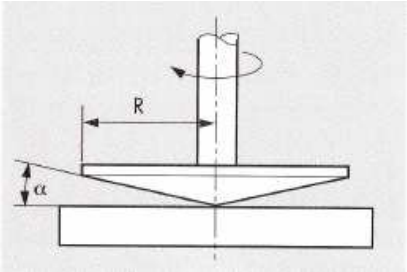

Figure 2: Main part of a rheometer. The bottom plate is fixed and in the middle connect with cone-shaped plate. The sample is placed into the gap between the plates. Cone-shaped plate is turning with shear rate $\dot{\gamma}$, which is changed from 0,01 s^{-1} to 1000 s^{-1} depending on the test. *Figure taken from reference 1.*

Sample of paint is put into the gap between the plates seen in Figure 2. The gap (Figure 2 α) must be completely filled in order to attain correct results. Top plate turns and imputes shear stresses in the samples. Rheometer measures the force which is lost because of the structure and viscosity of the sample. All three tests, the rheology flow test, the temperature test and the frequency sweep test were done with a cone-and-plate measuring system [7]. From the results of those tests the most ideal combination (raw materials) for our system (paint) was determined. Temperature test and frequency sweep test are oscillatory tests, where samples are measured in the area LVE – linear viscoelastic range, where the sample structure is not deformed.

2.1. Flow test

The test describes the use of paint in practice. It starts with low shear rate (velocity) and then grows to maximum value. When shear rate grows the viscosity drops and is comparable with the brush, when paint is stretched on the surface. After stretching paint at the end on the surface there is low input shear rate. That can be compared with rheology flow graph after the shear rate drops and with which we can measure how viscosity increases (structure of the paint is forming). Flow curve is made in 3 steps: Number 1 from Fig. 3.1 shear rate $\dot{\gamma}$ rises from 0,01 s^{-1} to 1000 s^{-1} with 40 points in 348 seconds. Number 2 from Fig 3.1 describes $\dot{\gamma}$ with constant shear rate

1000 s^{-1} with 2 points in 30 seconds. Number 3 from Fig 3.1 describes decrease shear rate $\dot{\gamma}$ from 1000 s^{-1} to 0,01 s^{-1} with 40 points in 207 seconds.

2.2. Temperature test

In this test we measured the change in system by warming up the sample. The best sample is the one, whose viscosity or other rheological parameters (G´- storage modulus, G˝- loss modulus) do not increase with temperature. This test is oscillatory test where frequency (1,6 Hz) and deformation (γ = 2 %) are constant. Temperature increases from 10 ^{o}C to 100 ^{o}C at rate of 6,75 ^{o}C/min. Test lasts 800 seconds and it measures 40 points (Fig. 3.2).

2. 3. Frequency sweep test

The test shows what can happen with the sample in the future by storage. It shows whether the pigment in the sample will settle down. It is not possible to predict the time of sedimentation but it is possible to predict which sample will sediment before another. Test is done in LVE area with constant deformation (γ = 2 %) and changing frequency from 95 Hz to 0,008 Hz. Test describes by very low frequency if the sample has gel structure G´>G˝ or not.

3. Results and discussion

Results show a connection between rheology flow test, temperature test and frequency sweep test. Rheology flow test graph shows dependence of viscosity on the shear stress. When the shear stress increase the viscosity decreases. From many measurements it was seen that when paint is applied on the surface with a brush, it is done with shear rate lower than 1000 s^{-1}. This was our top limit for the shear stress (Figure 3).

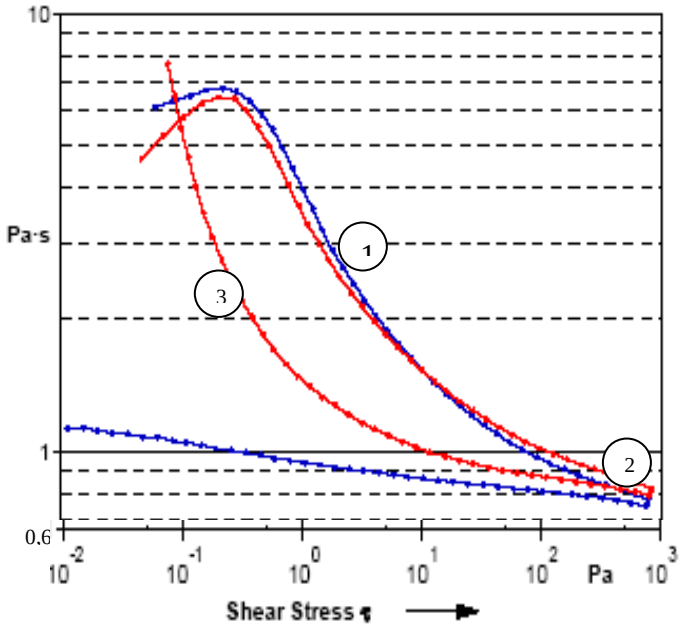

Figure 3: Figure shows the change of viscosity with increasing shear stress. Figure shows also effects on viscosity with decreasing shear stress. Numbers 1, 2 and 3 shows the areas. Number 1 introduces the area which is connected to frequency sweep test. Number 2 introduces the area of application shear stress. Number 3 introduces the area which is connected to temperature test.

In Figure 3, apparent differences between samples can be seen. The difference between samples is seen when shear stress decreases. Red line shows for the sample that it goes to starting position to soon (viscosity is growing faster). Blue line is

describing a sample on Figure 3, point 3 results shows that viscosity is growing slow, when shear stress drops. The result which describes sample with red line (by adding on the surface) proves that it is not possible to get good leveling as it is with sample which describes blue line. Since viscosity did not change more than 1 Pa·s in 207 seconds (Figure 3 Number 3) suggests that we have had a stable system with low interaction between participles of pigment. The only difference between blue and red samples from the graph is in dispersing agent and that difference has an influence on the interaction between particles. Those interactions are stronger in red sample and this is why leveling was also not confirmed by painters (when they put the sample on the surface).

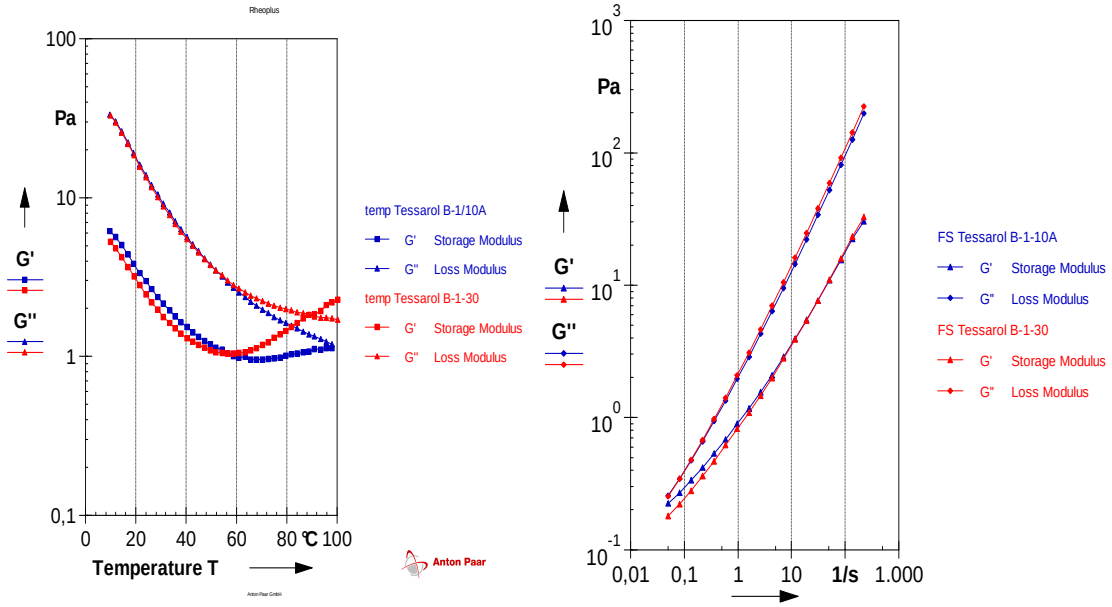

Figure 4: The left graph shows temperature tests with G' and G'' values of two types of samples, which are heated up to 100°C. The right graph shows frequency dependence of the G' and G'' values of the same two types of samples.

Temperature test (Figure 4) shows the dependence of sample's behavior on changing the temperature. In Figure 4, G´ starts increasing when temperature is 55°C that is for sample which is described with red line. The G´ from the sample which is described with blue line does not increase so much with higher temperature as in the case of red sample. The results of temperature test shows that interactions between particles are stronger in the sample which is described with red line. This accelerated test for paints can be correlated to the paint properties after long periods of time (flocculation of the pigment after long time). That is also confirmed with flow test (Figure 3) where number 3 shows differences between samples in that area.

In Figure 4, we show the result for frequency sweep test for two samples. The Fig. 3.3, shows that G'' will stay below G' at low frequency which means that paint samples have strong structure that prevent pigment sedimentation, after long period of time. Minimal differences were obtained between the samples. The results in Figure 4 show that both samples have strong structure. That is also confirmed with flow test (Figure 3) where number 1 shows no difference between samples in that area.

This connection between the three methods is not true always (for all liquids) but it turns out that stands for our decorative paint.

4. Conclusions

Rheology testing of the products is important when rheology has influence on the main property of the product, which is the case for paints. Flow test graphs help us in obtaining results faster. It was determined that the only test which is needed to obtain the rheology properties (for our paint) is the rheology flow test. Rheology flow test shows the behavior of paint when paint is used on the surface. It also shows the stability which is normally seen in other tests (temperature test, frequency sweep test). Problem with sedimentation can be seen with frequency sweep test but this test was not needed for our samples since results of frequency sweep test were predicted in the flow test. Rheology flow test graph also explains interaction between participles of pigment and stability of the sample that is with values of viscosity when shear stress drops. Stability of the system can also be measured with the temperature test. However, it was not required it for our samples, since the stability could be determined with the flow test. We used that fact always when we were using more or less the same raw materials just in different volume. Our results will enable faster and more precise determination of rhelogy properties.

5. References

[1] T. G. Mezger, *The Rheology-Handbook*, Vincentz Verlag, Hannover, 2002.

[2] G. Schramm, *A practical approach to Rheology and Rheometry*, 2nd Edition, Thermo Electron Karlsruhe, 2004.

[3] K. Holmberg, *High Solids Alkyd Resins*, New York, 1987.

[4] H. Krister, *High Solids Alkyd Resins*. Books in Solis and the Environment, library of Congress Cataloging-in-Publication Data, New York, 1987.

[5] M. Žumer, U. Florjančič, A. Zupančič Valant, A. Mesec, *Seminar iz aplikativne reologije*, Fakulteta za kemijo in kemijsko tehnologijo; Ljubljana, 1997.

[6] A. Zupančič Valant, *Uvod v reologijo*, Fakulteta za kemijo in kemijsko tehnologijo; Skripta za interno uporabo, 2002.

[7] H. A. Barnes, *A Handbook of elementary rheology*, University of Wales, Institute of Non-Newtonian Fluid Mechanics, 2000.